Catalysis Science & Technology

Ligand-coordinated Ir Single-atom Catalysts Stabilized on Oxide Supports for Ethylene Hydrogenation and Their Evolution under a Reductive Atmosphere

Journal:	*Catalysis Science & Technology*
Manuscript ID	CY-ART-06-2020-001132.R1
Article Type:	Paper
Date Submitted by the Author:	24-Dec-2020
Complete List of Authors:	Chen, Linxiao; Indiana University Ali, Iyad; Indiana University, Dept. of Chemistry Sterbinsky, George; Argonne National Laboratory Zhou, Xuemei; Indiana University Bloomington, Dept. of Chemistry Wasim, Eman; Indiana University, Dept. of Chemistry Tait, Steven; Indiana University, Dept. of Chemistry

Ligand-coordinated Ir Single-atom Catalysts Stabilized on Oxide Supports for Ethylene Hydrogenation and Their Evolution under a Reductive Atmosphere

Linxiao Chen,[1,†] Iyad S. Ali,[1] George E. Sterbinsky,[2] Xuemei Zhou,[1,‡] Eman Wasim,[1] and Steven L. Tait[1,*]

[1] Dept. of Chemistry, Indiana University, Bloomington, Indiana 47405, USA

[2] Advanced Photon Source, Argonne National Laboratory, Lemont, Illinois 60439, USA

* E-mail: tait@indiana.edu, Tel: +1-812-855-1302

[†] Present address: Institute for Integrated Catalysis, Pacific Northwest National Laboratory, Richland, Washington 99352, USA

[‡] Present address: School of Chemical Engineering, Sichuan University, No. 24 South Section 1, Yihuan Road, Chengdu, 610065, P.R.C.

Abstract

In this work, we present a novel series of oxide-supported Ir-ligand single-atom catalysts (SACs) for ethylene hydrogenation. The SACs were created by a metal-ligand self-assembly strategy developed by our group, using one of two ligands, either 1,10-Phenanthroline-5,6-dione (PDO) or 3,6-Di-2-pyridyl-1,2,4,5-tetrazine (DPTZ), on powder supports of either CeO_2 or MgO. Characterization by XAS, XPS, and CO adsorption proved that Ir exist principally as highly uniform, cationic single-atoms . Ir SACs show significantly higher durability and metal utilization efficiency than Ir nanoparticle (NP) catalysts during ethylene hydrogenation at 100 °C, as well as excellent stability, as no Ir aggregates were detected after > 10 h reaction. The activity can be tuned by ligand and support effects: PDO and CeO_2 are superior to DPTZ and MgO, respectively. This tunability is attributed to differences in H_2 activation capability, which results from differences in support reducibility, electron density on Ir, and, potentially, the local coordination environment of Ir. The Ir SACs lose H_2 activation activity either under inert gas or under H_2. Through XPS and *in situ* XAS studies, we attributed the former to the reversible loss of Ir hydride, which is the active species for H_2 activation, and the latter to irreversible over-hydrogenation and loss of Ir−O/N coordination. This work presents a new type of Ir hydrogenation SACs that are more durable, efficient, and tunable than supported Ir NPs, while more stable than homogeneous Ir complexes. It also offers fundamental understanding regarding the ligand and support effect, as well as the evolution of Ir single-atoms under H_2, instructing future design of stable, effective hydrogenation SACs.

Keywords: single-atom catalysts; ethylene hydrogenation; Ir catalysts; *in situ* evolution

Introduction

Heterogeneous catalysts are ubiquitous in modern industrial chemical processes. Although they allow easy separation and recovery from the reactions stream, heterogeneous catalysts are typically challenged by a low fraction of active sites and non-uniform chemical environments of metal centers, which lead to lower metal site utilization and poorer selectivity than homogeneous catalysts. Heterogeneous single-atom catalysts (SACs) are widely regarded as promising solutions to these challenges by combining advantages of homogeneous and heterogeneous catalysts.[1-5] Ideally, complete site isolation on SACs allows 100% metal utilization efficiency and the uniformity of metal sites offers improved selectivity. Nevertheless, to fabricate stable SACs, one must overcome the thermodynamic driving force of metal atom aggregation under reaction conditions. Several SAC approaches are being developed,[6] including surface organometallic chemistry,[5, 7-9] anchoring through specific support sites or linkers,[10-15] zeolites and metal-organic frameworks,[16, 17] single-atom alloys,[18-21] and small oxide particle supports.[22, 23] Despite this progress, SACs are often limited in metal loading or by the loss of metal-support interaction, in the case of anchoring or tethering by molecular linkers. To achieve high loading while maintaining the direct metal-support contact, our group first applied metal-ligand self-assembly, a strategy traditionally studied on single crystal model surfaces for isolated metal sites,[24-29] to build highly stable metal-ligand SACs on high-surface-area oxide powders.[30, 31] Rationally designed ligands with suitable pockets and oxidizing potential ensure the stability of high-loading cationic metal single-atoms, even at elevated temperature. The broad ligand space offers significant potential for fine-tuning chemical character of metal centers. We demonstrated the advantages of these ligand-coordinated SACs by showing improved performance in alkene hydrosilylation batch catalysis compared to commercial homogeneous Pt catalysts.[30, 31] In this

work, we apply the novel, promising metal-ligand SAC strategy to the important problem of ethylene hydrogenation in a flow reactor.

Hydrogenation catalysis is well-studied due to its importance in fuel production,[32-35] large-scale chemical manufacturing,[36-38] and synthetic organic chemistry.[39-41] The development of hydrogenation catalysts with low cost, high durability, and high selectivity is highly desired. SACs of late-transition metals, such as Pt,[42] Pd,[12, 43] Ir,[44-48] Ni,[49] and Co,[50, 51] have been explored toward this goal. Compared with traditional nanoparticle (NP) catalysts, the absence of adjacent metal sites in SACs offers improved selectivity by limiting the adsorption of unsaturated functional groups and the activation of H_2. Ir is of particular interest because, despite its success in homogeneous hydrogenation catalysis,[52-57] it is much less explored in heterogeneous hydrogenation catalysis.[44-46] Only examples of Ir hydrogenation SACs are from Gates, *et al*., created by surface organometallic chemistry and ligand exchange. The Ir SACs exhibited potential for selectivity enhancement,[45, 47] and regulation of electronic properties by the support[44, 46] or the ionic liquid sheaths was investigated.[45, 47] Nevertheless, such Ir SACs are limited to low-temperature application, and the behaviors of Ir single-atoms under high-temperature reducing atmosphere remains elusive. Also, the tuning of catalytic performance of Ir SACs using organic ligand, which represents a broader space than the support, is not exploited.

We report the development and detailed characterization of Ir-ligand hydrogenation SACs on powdered oxide supports with a different strategy. We evaluated the activity, stability, and support/ligand effect of the SACs using ethylene hydrogenation. Steady hydrogenation activity was observed and Ir single-atoms do not aggregate during catalysis even at elevated temperature. The significant ligand and support effects are attributed to differences in H_2 activation capability. The structure of Ir single atoms is dynamic under H_2, leading to changes in H_2-D_2 exchange

activity. This work demonstrated a novel metal-ligand strategy to create Ir SACs, which exhibit potential as efficient, durable, stable, and tunable hydrogenation catalysts. In addition, understanding the evolution of Ir single-atoms under H_2 contributes to the stability enhancement.

Experimental Methods

Synthesis of Ir-ligand SACs. Ir SACs were synthesized using a one-step impregnation method developed by our group.[30] For the example of Ir-DPTZ/CeO_2, 0.0108 g DPTZ were first dissolved in 20 mL 1-butanol. 0.3 g CeO_2 powders (BET surface area $\approx$ 5 $m^2 \cdot g^{-1}$) were added to the DPTZ solution, and the mixture was stirred for 2 h. Then, 5 mL 1-butanol containing 0.0027 g dissolved $IrCl_4$ (0.5% Ir wt%) was added to the mixture dropwise in 30 min. The final volume of the mixture was ~ 30 mL. This mixture was stirred at room temperature for 24 h, and the solvent was slowly evaporated by flowing dry air over the mixture overnight. Resulted powders were washed with H_2O and DCM for multiple times sequentially to remove free Ir and DPTZ. Powders obtained after drying were fresh Ir-DPTZ/CeO_2 SAC. For Ir-PDO SACs, 0.0108 g DPTZ was replaced by 0.0101 g PDO, and H_2O was used instead of 1-butanol as the solvent due to solubility concerns. For MgO-supported SACs, CeO_2 was replaced by MgO (BET surface area $\approx$ 5 $m^2 \cdot g^{-1}$) of the same mass. All fresh Ir SACs are light-yellow powders. Supported Ir NP catalysts were synthesized as references following similar procedures with H_2O as the solvent, except for no ligand was added. Ir NP catalysts were reduced at 400 °C for 4 h with H_2.

Characterization of Ir SACs by X-ray absorption spectroscopy (XAS). XAS measurements were performed at the 9-BM beamline at the Advanced Photon Source of Argonne National

Laboratory. The monochromatized X-ray energy was calibrated with the L3-edge of a Pt foil (11562.76 eV). X-ray absorption spectra were measured at the Ir L3-edge (11215.2 eV), from 10965 to 11957 eV. For *ex situ* measurements, samples were pressed into pellets with d $\approx$ 7 mm. For all supported Ir SACs, fluorescence data were collected and used for analysis. X-ray absorption spectra were also measured on Ir-containing compounds $Ir_4(CO)_{12}$, $Ir(CO)_2(AcAc)$, $[Ir(COD)Cl_2]_2$, $K_3IrCl_6 \cdot xH_2O$, and $Na_2IrCl_6 \cdot xH_2O$ (diluted with poly-ethylene glycol when making pellets) as standard references (Fig. S5); transmission data were used for analysis of them. For *in situ* measurements, Ir-PDO/MgO was pressed into self-standing pellets inside of a heat-conducting sample holder. The total gas flow in the reaction chamber was always 150 SCCM. All XAS data were processed and modelled by the Athena/Artemis software package.[59] Details regarding EXAFS fittings are included in the SI.

X-ray photoelectron spectroscopy (XPS). X-ray photoelectron spectra were measured at Indiana University (IU) Nanoscale Characterization Facility with a PHI Versaprobe II XP spectrometer using a monochromated Al X-ray source. Ir 4*f*, Ce 3*d*, N 1*s*, C 1*s*, O 1*s* and Cl 2*p* regions were collected. The binding energy was corrected with the C 1s peak (284.8 eV).

CO adsorption IR. CO adsorption experiments were carried out in a DiffuseIR environmental chamber (PIKE Technologies, 162-4160, HTV) using a Nicolet Magna 550 FT-IR spectrometer. An IR background was collected after flowing pure Ar (40 SCCM) over fresh samples at room temperature for 1 h. Then each sample was treated with 10% CO in Ar for 40 min before an IR spectrum was collected. CO gas was purged out of the chamber by pure Ar for 1 h, and another IR spectrum was collected. Each spectrum is an average of 500 scans. All IR spectra in this work were presented in Kubelka-Munk units.

Transmission electronic spectroscopy (TEM). TEM imaging was performed at Indiana University Electron Microscopy Center, with a JEOL JEM 3200FS microscope.

Inductively coupled plasma mass spectrometry (ICP-MS). ICP-MS measurements were performed at IU Department of Earth & Atmospheric Sciences with an Agilent 7700 quadrupole ICP-MS instrument. Solid catalysts were treated with aqua regia to dissolve all Ir, and the resulted solutions were analyzed after dilution.

X-ray diffraction (XRD). XRD experiments were performed at IU Molecular Structure Center with a Panalytical Empyrean Diffractometer equipped with a Cu Kα X-ray source and a transmission-reflection spinner. The 2θ range was from 20° to 90°, with a step of 0.02°.

H_2/D_2 exchange. H_2-D_2 exchange experiments were conducted in a customized flow reactor that was described in our previous publications.[60, 61] The mixture used contains 10% H_2 and 10% D_2 at a total flow rate of 40 SCCM balanced with Ar. For standard measurements, the amount of Ir SACs was varied between 3 and 7 mg to ensure the total amount of Ir sites is identical among samples, and HD yield is less than 20%. Samples were diluted with SiO_2 to a total mass of 70 mg to increase the bed length and minimize the channeling effect. The steady-state HD yield at 100 °C was quantified by a mass spectrometer at m/z = 3), the equilibrium intensity of which was quantified using 100 mg reduced 5% Pt/Al_2O_3 catalyst (Alfa Aesar) at 100 °C. Flowing the mixture through an empty catalyst bed yielded no HD formation at 100 °C. For deactivation experiments, 100 mg fresh catalysts were used, with other parameters kept identical.

OH/OD exchange. OH/OD exchange experiments were performed in the same *in situ* DRIFTS chamber as CO adsorption. Each sample was heated to 100 °C under Ar and treated with 20% H_2 in Ar at 100 °C for at least 1 h, before the IR background was collected. The flow

was then changed to 10% H_2 and 10% D_2 in Ar, and an IR spectrum was collected after 10 min. Each spectrum is an average of 200 scan.

Catalytic ethylene hydrogenation. ethylene hydrogenation was performed in the same flow reactor as H_2-D_2 exchange.[60] 100 mg catalysts were used unless otherwise specified. To avoid the local heating and channeling effects, the catalyst bed was diluted with 100 mg SiO_2. The normal reaction mixture contains H_2 : C_2H_4 : Ar = 2 : 1 : 7 with a total flow of 40 SCCM. Unless otherwise specified, the reaction temperature is 100 °C and the total pressure in the catalyst bed is close to ambient pressure. During E_a measurements, the reaction temperature was varied between 70 °C and 120 °C. During reaction order measurements, H_2 or C_2H_4 partial pressure was varied by changing the fraction of the corresponding gas in the reaction mixture. A quadrupole mass spectrometer was used as the detector, and intensities at all *m/z* values were normalized to *m/z* = 40 intensity (from Ar). Two *m/z* values, 30 and 26, were monitored in the SEM mode, and their background intensities were measured using a gas mixture equivalent with the reaction mixture without H_2. The formation rate of hydrogenation product ethane was quantified by the intensity at *m/z* = 30 (the contribution of ethylene is negligible at this *m/z* ratio). Contribution from ethane to *m/z* = 26 was calculated from its *m/z* = 30 contribution and the ratio between the two, which was measured using an ethane/Ar flow. Contribution to *m/z* = 26 intensity from reactant ethylene was obtained by subtracting ethane contribution from total intensity, which was then used to calculated ethylene conversion. Intensity at *m/z* = 26 with no ethylene conversion was obtained with an empty catalyst bed at room temperature, so that conversions and reaction rates can be calculated. No other products, such as C_4 hydrocarbons from C−C coupling were detected in all experiments.

Results

1. *Synthesis and characterization of Ir-ligand SACs*

We have applied a unique metal-ligand complexation strategy, previously developed by our group,[30, 31] to create Ir-ligand SACs on oxide supports. As described above, we used a modified wet impregnation process with $IrCl_4$ and one of the two organic ligands: 3,6-Di-2-pyridyl-1,2,4,5-tetrazine (DPTZ, **Fig. 1**), or 1,10-Phenanthroline-5,6-dione, (PDO, **Fig. 1**) to load catalyst onto CeO_2 or MgO powders in one single step, followed by room-temperature solvent evaporation and rinsing with H_2O and DCM. Both ligands are known to have suitable binding pockets and oxidizing potentials to stabilize cationic metal single-atoms[24-26] and replace Cl during the synthesis, but offer different coordination environments to tune Ir sites. CeO_2 and MgO were chosen to investigate the support effect due to their reducibility and electron-donating properties, respectively.[62, 63] This novel strategy takes advantage of the ligand for higher metal loading and better tunability than other SACs, while maintaining the direct metal-support contact that is crucial in catalysis but often lost in immobilized organometallic catalysts. ICP-MS (**Table 1**) suggests that the Ir loading on the final SACs is impacted by the ligand and the support. Although both supports have limited surface area (~5 m^2/g), the Ir density on these SACs is up to 1.2 atom · nm^{-2}, which is quite high among noble metal SACs.

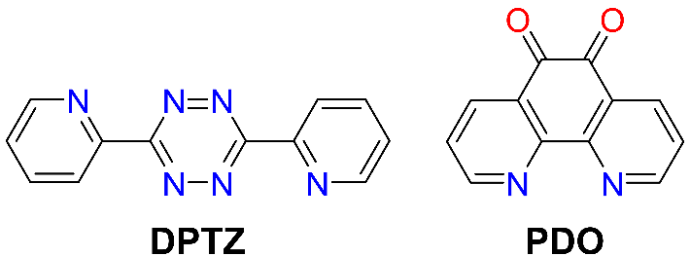

Fig. 1 Structures of ligands used to create Ir-ligand SACs

Table 1 Ir loadings on various Ir catalysts measured by ICP-MS as Ir weight percent (wt%). Note that in each case the same amount of Ir was used in the synthesis mixture (0.5 wt%), so these variations are due to differences in the choice of ligand.

Catalyst	Ir-PDO /CeO_2	Ir-DPTZ /CeO_2	Ir-PDO /MgO	Ir-DPTZ /MgO	Ir NP /CeO_2
Ir wt%	0.10	0.19	0.15	0.03	0.24

Ir-ligand SACs were characterized by Ir L3-edge X-ray absorption spectroscopy (XAS) to convincingly demonstrate the atomic dispersion of Ir and elucidate their local coordination environment. **Fig. 2a-c** shows extended X-ray absorption fine structure (EXAFS) of three fresh Ir-ligand SACs, in *R*-space . The first-shell coordination of Ir is completely described by models including only Ir−O/N (Ir−N and Ir−O are too similar in distance to be considered separately[30]) and Ir−Cl scattering paths, while Ir−Ir and Ir−O−Ir paths (**Fig. 2d**) are clearly absent. Therefore, Ir exists predominantly as single-atoms bound with N (from the ligand), O (from PDO ligand and/or the support), and Cl (from $IrCl_4$ precursor). The total coordination number of Ir on all three fresh SACs is at least 6 (**Table 2**), suggesting a crowded coordination sphere. This is also supported by the high ligand : Ir and Cl : Ir ratios calculated from XPS (**Table S3**).

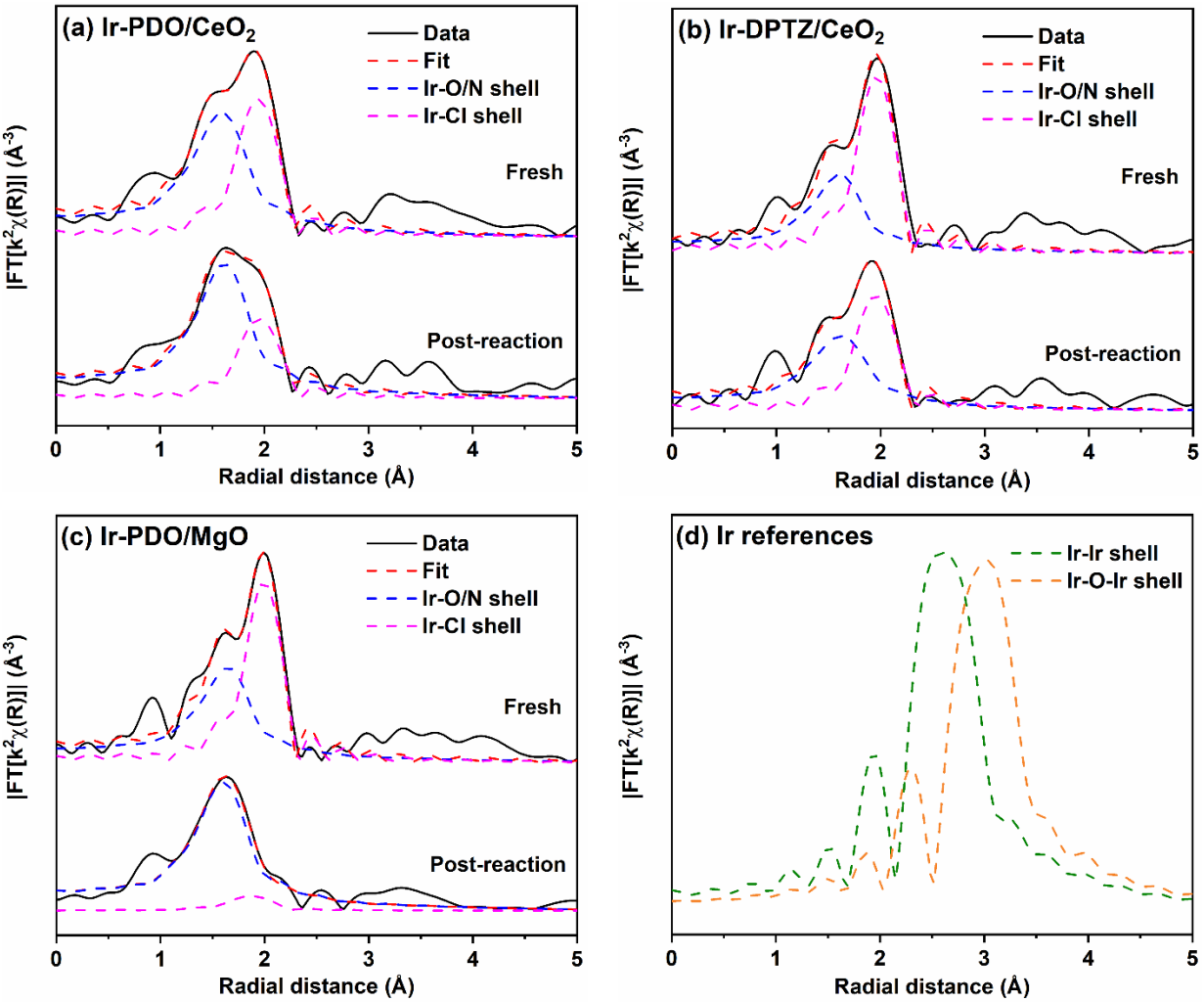

Fig. 2 EXAFS Fourier transform amplitudes of fresh and post-reaction Ir-ligand SACs in *R*-space (Fourier transform, k^2-weighted, but not phase-corrected) with first-shell fittings: (a) Ir-PDO/CeO_2, (b) Ir-DPTZ/CeO_2, and (c) Ir-PDO/MgO. See **Fig. S1** for fresh Ir-DPTZ/MgO and **Fig. S2a-S2b** for the *k*-space and *R*-space imaginary component spectra corresponding to panels (a)-(c). (d) Ir−Ir and Ir−O−Ir scattering paths calculated by FEFF from Ir and IrO_2, respectively, presented for comparison. The absence of Ir−Ir or Ir−O−Ir paths in (a), (b), and (c) indicates that Ir exists predominately as single-atoms pre- and post-reaction. Fitting parameters are in **Tables 2** and **S1**. Note that intensity above 3 Å is mainly due to second shell interactions with C (in the ligand) and Ce or Mg (in the support).

Table 2 XANES white line intensity and EXAFS coordination numbers for Ir SACs.

		White line intensity	N(Ir−O/N) [a,b]	N(Ir−Cl) [a,b]
Ir-PDO/CeO_2	Fresh	2.86	5 (1)	2.3
	Post-reaction	2.74	5.7 (0.7)	1.3
	Post-H_2	2.76	6 (3)	1.3
Ir-DPTZ/CeO_2	Fresh	2.77	4 (1)	3.3
	Post-reaction	2.65	4.7 (0.4)	2.2
Ir-PDO/MgO	Fresh	2.69	4.1 (0.9)	2.8
	Post-reaction	2.61	5.4 (0.9)	0.3
	Post-H_2	2.15	0.9 (0.2)	1.1
Ir-DPTZ/MgO	Fresh	2.83	3.5 (0.4)	3.7

[a] For all fittings, S_o^2 was fixed to 0.85 based on fittings results of K_3IrCl_6 and Na_2IrCl_6 standards.
[b] A complete set of all fitting parameters and more detail about the fitting procedure are provided in **Table S1** and related discussion in the supporting information.

X-ray photoelectron spectroscopy (XPS) suggests that Ir single atoms are cations with uniform oxidation state. Fresh Ir SACs show narrow Ir 4*f* peaks with binding energy (BE) between Ir(IV) and Ir(0) (**Fig. 3**). For both CeO_2-supported Ir SACs, the FWHM of the Ir $4f_{7/2}$ peak (1.6, **Fig. 3a** and **3c**) is close to that of $IrCl_4$ (FWHM = 1.5, **Fig. 3g**), suggesting highly uniform oxidation states. MgO-supported Ir SACs exhibit wider Ir 4*f* peaks (FWHM = 2.0 and 2.3, **Fig. 3e-3f**), but they are still narrower than those from supported Ir NPs (FWHM = 2.4, **Fig. 3h**). Determining exact Ir oxidation state from X-ray spectroscopy is difficult because the BE of Ir $4f_{7/2}$ XPS peak is not highly sensitive to Ir oxidation state (~61.0 eV for 0 and ~62.8 eV for +4), and in X-ray absorption near edge structure (XANES) of Ir standards, neither white line

intensity nor edge position correlates well the oxidation state (**Fig. S5** and following discussion). XPS also clearly detects N from the ligands, and after rinsing, very little ligands stay on the supports without Ir,[64] confirming the Ir-ligand coordination so that fresh samples are not simply adsorbed $IrCl_4$ (see **Table S3** for ligand:Ir). Similar with N, Cl are present on all samples but do not stick to the supports without Ir, confirming Ir-Cl coordination concluded from EXAFS. The fact that all Cl does not bind with supports without metal also eliminates the impacts of support-bound Cl to catalysis.

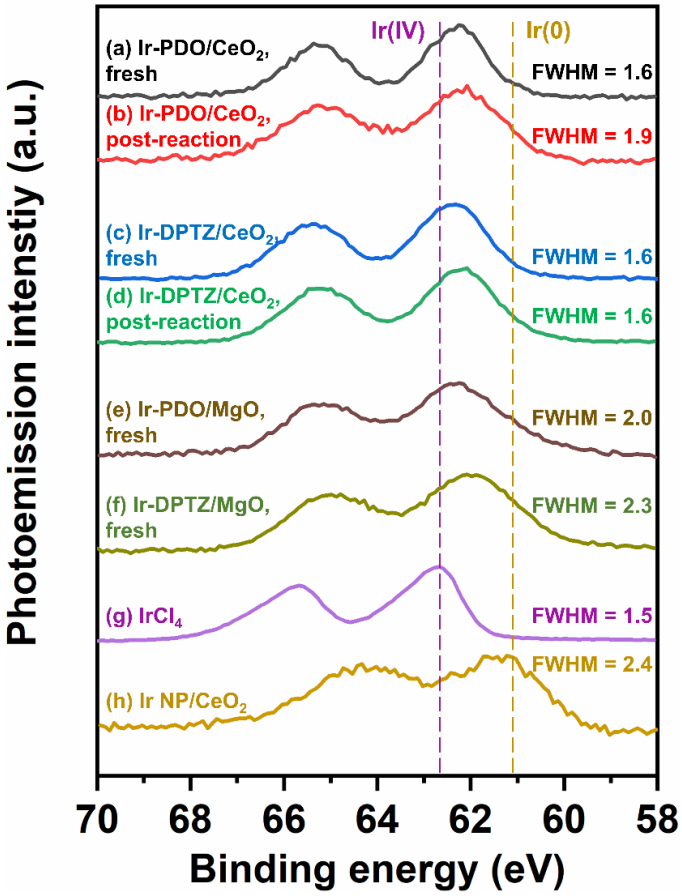

Fig. 3 XP spectra in Ir 4*f* region of various Ir samples and FWHM of $4f_{7/2}$ peaks: (a) fresh Ir-PDO/CeO_2 SAC, (b) sample (a) after ethylene hydrogenation at 100 °C, (c) fresh Ir-DPTZ/CeO_2 SAC, (d) sample (c) after ethylene hydrogenation at 100 °C, (e) Ir-PDO/MgO SAC, (f) Ir-DPTZ/MgO SAC, (g) pure Ir precursor, $IrCl_4$, (h) Ir NP/CeO_2 catalyst (Ir/CeO_2 reduced by H_2 at 400 °C).

The structure of atomically dispersed Ir was further examined by CO adsorption IR (**Fig. 4**). Exposing bare CeO_2 to CO does not yield any peaks between 1900 and 2200 cm^{-1}. CO adsorption on CeO_2-supported, reduced Ir NPs leads to three features: ~2070, ~2080, and ~2020 cm^{-1} (**Fig. 4**, black). Based on multiple prior studies on reduced Ir/M_xO_y[65-69], they are assigned to linear CO on metallic Ir NPs, symmetric and asymmetric vibration of $Ir^{m+}(CO)_2$ species. The sample has Ir^{m+} species for two reasons: 1) aforementioned studies showed that a fraction of Ir remain cationic after reduction, and 2) the sample has been exposed to air, causing surface oxidation. In contrast, on both Ir-PDO and Ir-DPTZ SACs (blue and red), no intensity at 2070 cm^{-1} is observed. All peaks for the Ir-ligand SACs are above 2080 cm^{-1}, consistent with linear CO on Ir^{m+}, confirming that Ir are predominantly cationic single-atoms, a conclusion strongly supported by EXAFS and XPS. The absence of the symmetric/asymmetric peak splitting implies only one CO adsorbs on each Ir, likely due to the crowded coordination sphere, consistent with our EXAFS results (**Table 2**). The vibration frequency of the Ir^{m+}–CO feature is higher than prior reports for linear CO on Ir(I),[70] suggesting an Ir oxidation state greater than +1, possibly Ir(III).[71] The Ir^{m+}–CO peak shows asymmetry with multiple components, indicating Ir single-atoms are in different coordination environments, consistent with slightly wider XPS Ir 4*f* peaks than $IrCl_4$. MgO-supported Ir SACs do not adsorb any CO, which likely reflects its coordination saturation. The atomic dispersion of Ir on fresh Ir SACs is further supported by the absence of NP features from transmission electron microscopy (TEM, **Fig. S6a-S6b**) and powdered X-ray diffraction (XRD, **Fig. S6c**).

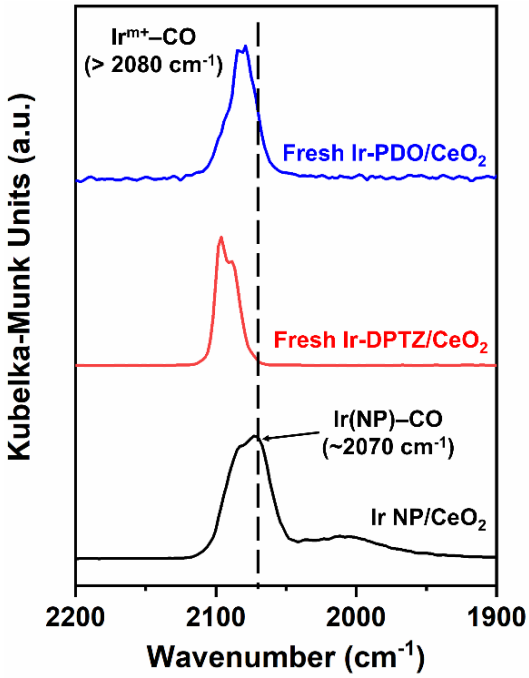

Fig. 4 CO adsorption IR spectra on fresh Ir catalysts. Each sample was exposed to 10% CO followed by Ar purging and IR measurement. Blue, red, and black curves represent results from Ir-PDO, Ir-DPTZ, and Ir NP catalysts on CeO_2, respectively.

2. Durability and Stability during Ethylene Hydrogenation

Ir-ligand SACs were tested for ethylene hydrogenation, a model hydrogenation reaction, at 100 °C. All SACs are active (**Table 3**) and remarkably durable. Ethane (C_2H_6) is the only product detected. The most active SAC is Ir-PDO/CeO_2, which after the induction period of ~1.5 h, shows steady C_2H_4 conversion for 13 h without noticeable deactivation (**Fig. 5**, red). In contrast, the same mass of Ir NP/CeO_2 starts with higher C_2H_4 conversion, but deactivates quickly within 6 h (blue) to a lower conversion than Ir-PDO/CeO_2. Beyond 10 h, Ir-PDO/CeO_2 SAC achieves slightly higher conversion than Ir NP/CeO_2 with only 40% as much Ir mass (same catalyst mass, 0.10 wt% Ir compared to 0.24 wt% Ir, **Table 1**), indicating higher metal utilization efficiency on SACs than NPs. This is due to the combination of atomic dispersion of Ir on SACs

and their strong resistance towards deactivation. Ir-PDO/MgO is also much more durable than Ir NPs, maintaining 85% of its original activity after 7 h at 120 °C (**Fig. 5**, green). Deactivation of metal NPs in ethylene hydrogenation has been attributed to the accumulation of hydrogen-deficient C_xH_y species with metal-carbon triple bonds.[72-75] The superior durability of Ir SACs is likely because the C_xH_y species require adjacent metal sites to form and stay on catalyst surfaces, and hence does not accumulate on single-atoms. The carbon poisoning effect on NPs is often associated with negative reaction orders with respect to C_2H_4. Non-negative C_2H_4 orders were observed on Ir-ligand SACs (**Table 3** and **Fig. S7c**), consistent with the improved durability. We note that Ir-ligand SACs lost most activity after a year of on-shelf storage, likely due to binding with O_2 in the air. Therefore, all experiments were performed within one month of the synthesis.

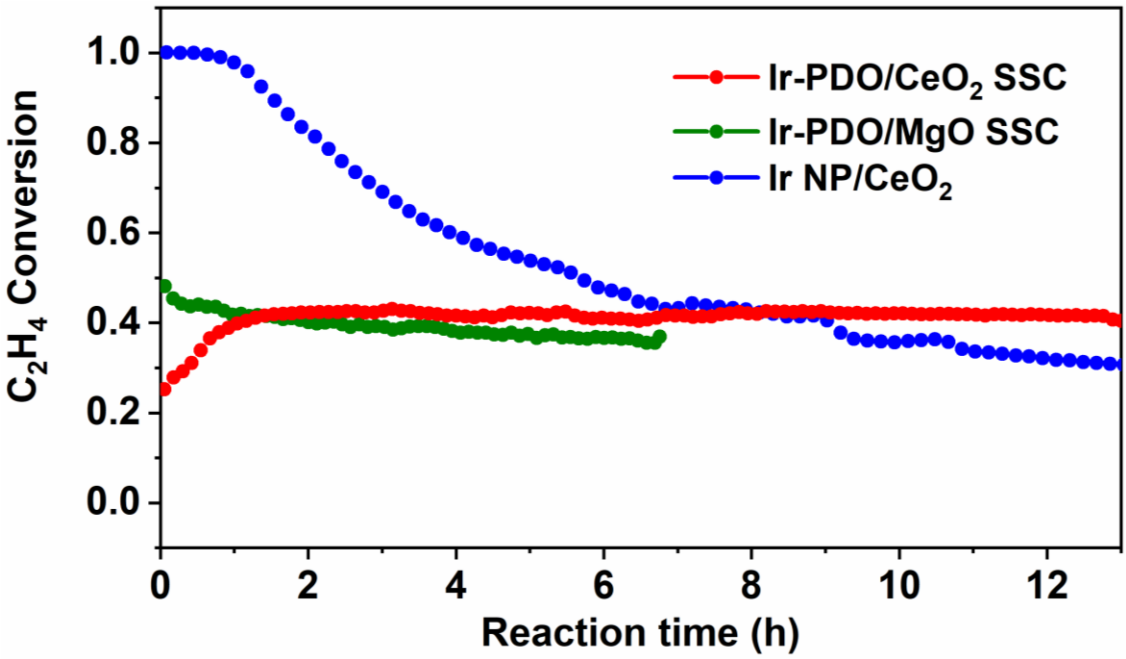

Fig. 5 Variations in ethylene conversion with time over Ir-PDO/CeO_2 SAC (red), Ir-PDO/MgO SAC (green), and Ir NP/CeO_2 (blue) during ethylene hydrogenation. Reaction condition: 100 °C (120 °C for Ir-PDO/MgO), 100 mg catalyst, H_2 : C_2H_4 : Ar = 2 : 1 : 7, with a total flow rate of 40 SCCM. The small dips in the blue curve are attributed to minor flow fluctuations.

Table 3 Ethylene hydrogenation activity and kinetic parameters of Ir SACs.

	Rate at 100 °C[a] (mmol C_2H_4 $\cdot s^{-1} \cdot g^{-1}$ Ir)	Apparent E_a[b] ($kJ \cdot mol^{-1}$)	Reaction order[c]		H_2-D_2 exchange fraction[d] (%)
			H_2	C_2H_4	
Ir-PDO/CeO_2	4.2	35 ± 4	0.44 ± 0.02	0.21 ± 0.01	33.2
Ir-DPTZ/CeO_2	1.8	56 ± 4	1.12 ± 0.06	0.52 ± 0.02	4.2
Ir-PDO/MgO	1.6	53 ± 2	0.98 ± 0.04	−0.02 ± 0.02	3.0
Ir-DPTZ/MgO	0.5	N/A	N/A	N/A	0.4

[a] Rate at 100 °C was measured at steady-state with 100 mg catalyst at ambient pressure. The reaction mixture contained H_2 : C_2H_4 : Ar = 2 : 1 : 7, with a total flow rate of 40 SCCM. The activity is presented as rate per g Ir instead of TOF because the conversion in some cases is above the threshold of a differential reactor. The most active supported Ir catalysts for this reaction in literature showed the rate of 3.5 (mmol $C_2H_4 \cdot s^{-1} \cdot g^{-1}$ Ir) at ~300 K under 333 mbar C_2H_4 and 666 mbar H_2.
[b] Apparent E_a was measured between 70 °C and 120 °C, with C_2H_4 conversion < 15%. Fitting plots can be found as Fig. S7a. Apparent E_a and reaction orders were not measured on Ir-DPTZ/MgO due to technical difficult associated with very low conversion.
[c] H_2 order was measured at 100 °C with constant P_{C2H4} at 76 Torr, P_{H2} between 76 and 302 Torr, and C_2H_4 conversion < 20%. C_2H_4 order was measured at 100 °C with constant P_{H2} at 152 Torr, P_{C2H4} between 38 and 152 Torr, and C_2H_4 conversion < 20%. Fitting plots can be found as Fig. S7b-c.
[d] H_2-D_2 exchange fraction was measured with identical Ir mass for all SACs at 100 °C, and values are reported relative to the equilibrium. The net H_2-D_2 exchange rate for Ir-PDO/CeO_2 is 0.14 (mmol $H_2 \cdot s^{-1} \cdot g^{-1}$ Ir), while the most active supported Ir catalysts in literature showed the H_2-D_2 exchange rate of 0.05 (mmol $H_2 \cdot s^{-1} \cdot g^{-1}$ Ir) at ~300 K.

To evaluate stability, three Ir-ligand SACs were characterized again after the reaction. In each case, neither Ir−Ir nor Ir−O−Ir path was observed in EXAFS (**Figs. 2a-2c**, **Table 2**), showing that Ir single-atoms do not aggregate under reaction conditions. In contrast, homogeneous Ir hydrogenation catalysts are often reduced and aggregate into poly-atomic Ir hydride during hydrogenation reactions.[52, 55, 56, 76] Therefore, the Ir-ligand SACs exhibit improved stability over their homogeneous counterpart. The SACs do show signs of minor reduction after the reaction: Ir 4*f* XPS peaks broaden, shift slightly to lower BE (**Fig. 3b** and **3d** compared with **3a** and **3c**), and XANES white line intensity decreases slightly (**Table 2**).

Nevertheless, both XAS and XPS of post-reaction Ir SACs are still consistent with cationic Ir single-atoms instead of Ir aggregates. No significant ligand loss was observed by XAS (Ir−O/N path in **Fig. 2** and **Table 2**) or XPS (ligand : Ir ratio in **Table S3**), indicating stable metal-ligand coordination. In contrast, both techniques show a significant loss of Cl from CeO_2-supported SACs after the reaction (decreases in *N*(Ir−Cl) from EXAFS fittings, **Table 2**, and drops in XPS Cl : Ir ratio, **Table S3**). We propose that the loss of Cl opens coordination vacancies to activate Ir SACs, accounting for the induction period, which is similar to our previous observations of Pt-ligand hydrosilylation SACs.[30, 31] Ir-PDO/MgO exhibits a significant drop in *N*(Ir−Cl) from EXAFS but no corresponding decrease in XPS Cl : Ir ratio, likely because basic MgO recaptures Cl as it leaves Ir as HCl. Overall, our results suggest that Ir single-atoms are highly stable under the reductive reaction condition: they remain coordinated with the ligand and are resistant towards aggregation.

3. Ligand and Support Effects

Our results suggest that the hydrogenation activity of Ir SACs is highly impacted by the ligand and the support. **Table 3** shows that on the same support, Ir-PDO SACs exhibit higher activity (higher reaction rate and lower apparent E_a) than Ir-DPTZ SACs. With the same ligand, Ir SACs are more active when supported on CeO_2 than MgO. Reaction orders with respect to H_2 and C_2H_4 also change significantly with the ligand and the support. These observations show that catalytic performance of Ir-ligand SACs can be tuned by the ligand and the support, and hence understanding these effects will instruct rational design of more efficient SACs. It has been suggested that H_2 dissociation is often the rate-determining step (RDS) of hydrogenation

reactions on SACs.[43, 44, 77] Therefore, we hypothesize that the ligand and the support regulate the hydrogenation activity of Ir SACs by tuning H_2 activation capability.

To examine this hypothesis, H_2-D_2 exchange was used to directly evaluate H_2 activation by Ir SACs. We flowed a 1 : 1 H_2/D_2 mixture at 100 °C through SACs with the same Ir mass. The steady-state H_2-D_2 exchange fraction (relative to the equilibrium) was quantified by monitoring HD formation rate with a mass spectrometer. Neither bare CeO_2 nor MgO exhibits detectable H_2-D_2 exchange activity. **Table 3** shows that, as hypothesized, the H_2 activation capability is affected by the ligand and the support, and there is a strong positive correlation between the hydrogenation activity and H_2 activation capability (**Fig. S8**). Our hypothesis is further supported by H_2 reaction order measurements (**Table 3**). It has been established that the RDS of ethylene hydrogenation is indicated by the H_2 reaction order, with 0.5-order suggesting H addition as the RDS (H_2 dissociation is equilibrated), while first-order indicates H_2 dissociation as the RDS. In **Table 3**, only Ir-PDO/CeO_2, the most active Ir SAC, exhibits a H_2 order close to 0.5 (0.44), implying equilibrated, fast H_2 dissociation . Two less active SACs show H_2 orders close to 1 (1.12 and 0.98), suggesting that H_2 dissociation is slow and the RDS of the reaction.

We further investigated the H_2 dissociation over Ir SACs by *in situ* IR. **Fig. 6** shows IR spectra acquired after 10 min H_2/D_2 flow. Neither CeO_2 nor MgO shows obvious surface −OH exchange by −OD, suggesting H_2 (D_2) does not dissociate easily on either support. For comparison, significant OH/OD exchange, represented by a negative O−H band and a positive O−D band (**Fig. 6b**), was observed on Ir SACs. Exchanged −OH are on support surfaces because −OH on Ir single atoms would only yield a narrow peak around 3600 cm^{-1},[78, 79] not the broad bands in **Fig. 6b**, which originates from −OH and water at various sites on oxide surfaces.[80-83] The results indicate that H_2 dissociation requires Ir but forms −OH on support surfaces, either

through heterolytic H−H cleavage at the Ir-oxide interface, or H spillover from Ir single atoms (Ir−H are not detected by IR, but XANES in **Fig. 7** confirms its presence under H_2). IR studies prove that oxide surfaces participate in H_2 dissociation or storage, further rationalizing the support effects.

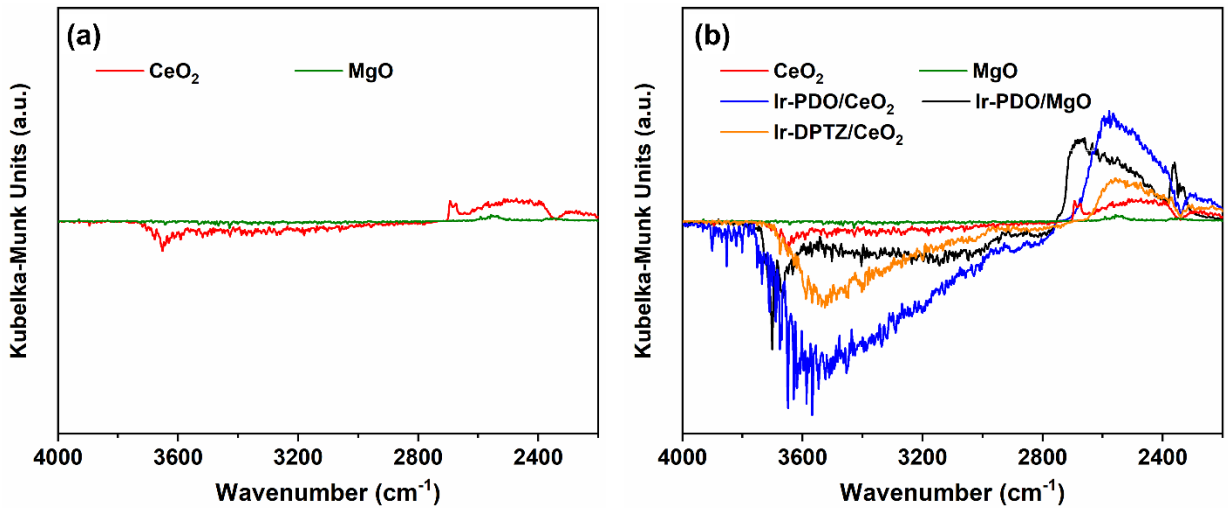

Fig. 6 OH/OD exchange on (a) bare oxide supports and (b) supported Ir SACs, detected by *in situ* IR after 10 min 10% H_2 + 10% D_2 flow at 100 °C. Before exposed to the H_2/D_2 mixture, each sample was treated with 20% H_2 for at least 1 h at 100 °C, and background spectra were collected before switching to H_2/D_2.

4. Dynamic Ir evolution under H_2

We also discovered that Ir single atoms evolves dynamically during H_2-D_2 exchange experiments. For example, fresh Ir-PDO/MgO SAC is not active for H_2-D_2 exchange until a quick activation when ramping up temperature under H_2/D_2 (**Fig. S9**). Then, when the temperature is held at 100 °C under H_2/D_2, the activity decreases gradually, which was also observed at 80 °C and 50 °C (**Fig. S9**). This H_2-induced deactivation cannot be reversed. On the other hand, treating the SAC with Ar overnight at room temperature leads to complete loss of H_2-D_2 exchange activity initially, but the activity gradually recovers under H_2/D_2 (**Fig. S9**), *i.e.*,

the Ar-induced deactivation is reversible. On CeO_2-supported Ir SACs, the reversible deactivation (Ar-induced) was also clearly observed, while the irreversible deactivation (H_2-induced) is almost negligible compared to Ir-PDO/MgO.

The changes in H_2-D_2 exchange activity indicate that the structure of Ir single atoms is dynamic under H_2. Therefore, the active sites for reactions involving H_2 might be formed and constantly changing *in situ*, thus understanding the evolution of Ir under H_2 is fundamentally critical. To achieve the purpose, *in situ* XAS was conducted on Ir-PDO/MgO SAC during H_2-He-H_2 treatment. The sample was heated to 100 °C under 20% H_2 in 0.75 h, and further treated with H_2 at 100 °C for 6 h. Then the gas was switched to He at 100 °C for ~ 5.5 h, after which H_2 was re-introduced for 6.5 h. During the entire experiment, Ir L3-edge X-ray absorption spectra were collected continuously, with results summarized in **Fig. 7** (see **Table S2** for EXAFS fitting parameters).

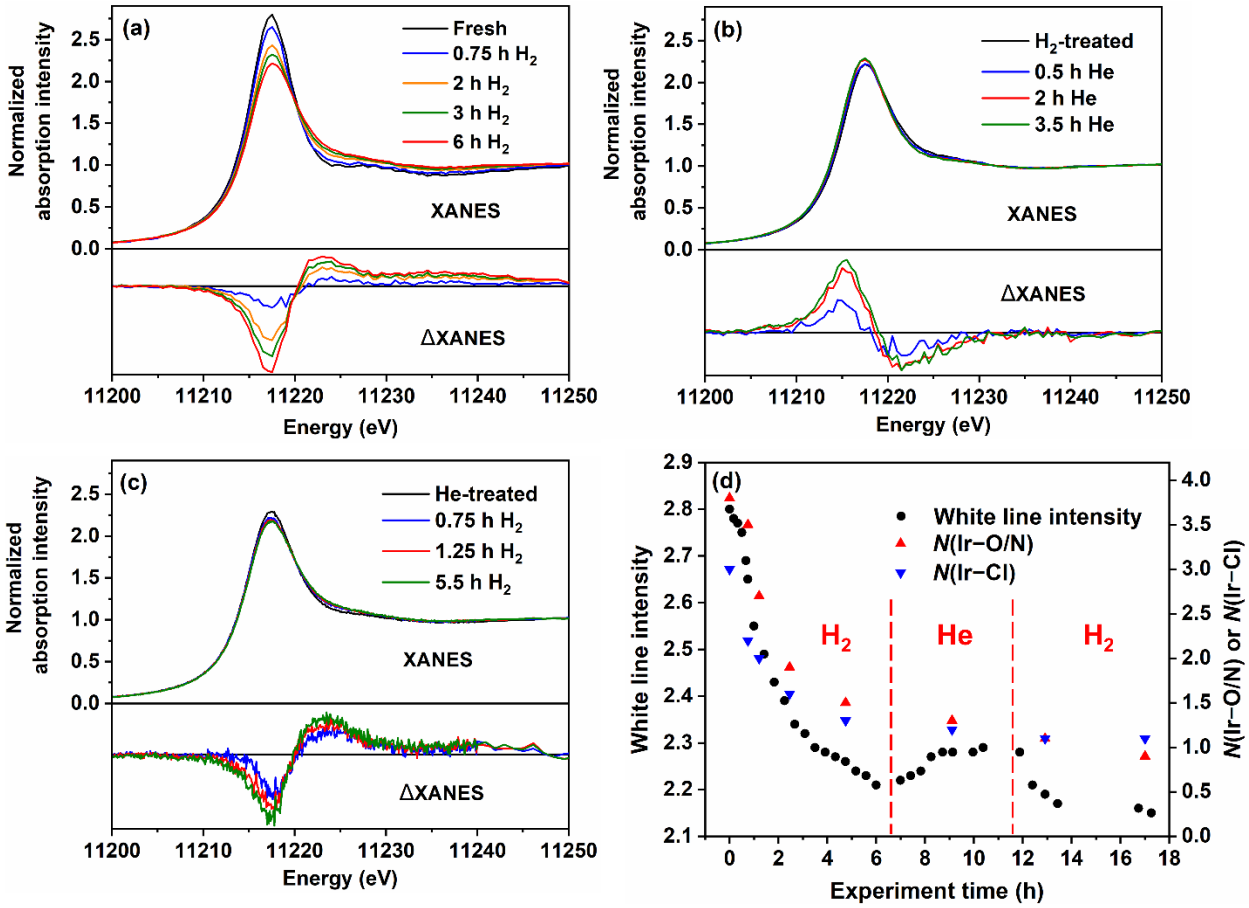

Fig. 7. Results from *in situ* Ir L3-edge XAS on Ir-PDO/MgO SAC during H_2-He-H_2 treatment. XANES region after normalization during (a) the initial H_2 stage (including heating to 100 °C from room temperature), (b) He stage, and (c) the second H_2 stage. In each graph, the black curve represents the initial status of the catalyst during each stage; for (b) and (c) the black spectrum is the same as the last spectrum in (a) and (b). Difference spectra (ΔXANES) are plotted in the bottom section of each panel with magnified intensity scaling. (d) XANES white line intensity (black dots), *N*(Ir−O/N) (red triangles), and *N*(Ir−Cl) (blue triangles) from EXAFS fitting during the entire experiment. Details of EXAFS fittings can be found in the SI as **Table S2**.

During the initial H_2 treatment stage, white line intensity, *N*(Ir−O/N), and *N*(Ir−Cl) decrease continuously, suggesting a loss of Ir−O/N and Ir−Cl coordination (**Figs. 7a** and **7d**). **Fig. 7a** also shows a slight absorption edge shift to higher energy and the appearance of a secondary feature centered at ~6 eV beyond the white line (highlighted in ΔXANES). This feature, with its well-defined position, has been recognized by multiple studies as a highly unique feature from the

metal−H σ* antibonding orbitals,[84-87] and no alternative explanation exists in literature. Therefore, it is strong evidence of metal hydride formation. The formation of Ir−H is consistent with decreased white line intensity, which is an indicator of Ir reduction. We note that the white line intensity drop could also be caused by the detachment of C=O (from PDO), which is implied by XPS (**Table S3**) and leads to less electron back donation to C=O π* orbitals. Overall, these results strongly indicate that under H_2, Ir−O/N and Ir−Cl coordination is gradually replaced by Ir−H. The replacement is associated with the initial activation and the following irreversible deactivation in H_2-D_2 exchange.

Under He, the Ir−H σ* feature is reduced in intensity (**Fig. 7b**), suggesting the partial disappearance of Ir−H. This is consistent with the slight increase in white line intensity (**Fig. 7d**) and the minor shift of absorption edge to lower energy. Meanwhile, no changes in *N*(Ir−O/N) or *N*(Ir−Cl) were observed beyond the uncertainty of EXAFS fittings, suggesting Ir−O/N or Ir−Cl coordination is not significantly interrupted. After re-introducing H_2, the white line intensity change is quickly reversed within 1 h (**Figs. 7c-7d**), indicating facile recovery of Ir−H. Then, the trends identified during the initial H_2 stage, *specifically, the* decrease in the white line intensity and *N*(Ir−O/N), continue as Ir further evolves under H_2. These results prove that the reversible deactivation is associated with the loss of Ir−H under inert gas, while the reactivation under H_2 is accompanied by re-formation of Ir-H bonds.

At the end of the experiment, white line intensity, *N*(Ir−O/N), and *N*(Ir−Cl) of Ir-PDO/MgO drop to 2.15, 0.9, and 1.1, respectively, significantly decreased from 2.80, 3.0, and 3.8 on the fresh sample (**Table 2**). Despite signs of reduction and coordination loss, Ir−Ir or Ir−O−Ir paths were not observed in EXAFS (**Fig. S3b**), again highlighting the strong resistance of Ir single-atoms towards aggregation. *Ex situ* XAS on post-H_2 Ir-PDO/CeO_2 (20% H_2, 15 h, 100 °C) also

has no contribution from Ir−Ir or Ir−O−Ir paths, *i.e.*, no Ir aggregates. Post-H_2 Ir-PDO/CeO_2 EXAFS exhibits a drop in *N*(Ir−Cl) from 2.3 to 1.3 compared to its fresh form, but only a slight decrease in white line intensity (from 2.86 to 2.76), and a similar *N*(Ir−O/N) within the uncertainty from EXAFS fittings (**Table 2**). In addition, its XPS exhibits a drop in Cl : Ir but not much change in PDO : Ir (**Table S3**). Comparing the results from Ir-PDO/CeO_2 and Ir-PDO/MgO, the significantly slower irreversible deactivation on the former is connected to less loss of Ir−O/N coordination and white line intensity drop. In summary, these results suggest that Ir single atoms form single-atom hydride without aggregation by replacing their first-shell Ir−O/N and Ir−Cl coordination. The single-atom Ir hydride are the active sites for H_2-D_2 exchange but are unstable under inert gas. Although replacing Ir−O/N by Ir−H is required for activating Ir single atoms, over-hydrogenation and loss of too much Ir−O/N coordination deactivates them.

Discussion

1. Ligand and support effects on hydrogenation activity of Ir SACs

We have demonstrated the ligand and support effects on Ir-ligand SACs in ethylene hydrogenation: PDO and CeO_2 outperform DPTZ and MgO respectively. We have also shown that these effects mainly originate from the H_2 dissociation step, which is supported by two facts: (1) hydrogenation activity and H_2 activation capability of Ir SACs are positively correlated and (2) the H_2 dissociation step in ethylene hydrogenation is faster than H addition only on Ir-PDO/CeO_2, the most active SAC (on less active SACs, H_2 dissociation is the RDS). H_2 dissociation on single atoms is generally slower than on NPs, due to the absence of adjacent metal sites for facile homolytic H−H cleavage, the widely recognized mechanism on most noble

metal NPs.[43, 44, 88] This also means a different mechanism is involved. Recent work demonstrated that on oxide-supported Ir and Pd single atoms, heterolytic H−H cleavage at the metal-oxide interface, generating metal hydride and a hydroxyl on oxides, is more favored than oxidative addition forming dihydride MH_2.[43, 88] This is consistent with the fact that upon Ir SAC exposure to H_2/D_2, we observed both surface OH/OD exchange with IR (**Fig. 6b**) and Ir−H with XANES (**Fig. 7a**), which support hydroxyl and hydride formation from H_2 dissociation respectively.

Therefore, we expect two potential factors leading to the support effect. First, the reducibility of CeO_2 facilitates heterolytic H_2 dissociation at the interface while MgO is not very reducible. Second, it has been established that electron-deficient Ir is more active than electron-rich Ir for H_2 activation.[44, 45] MgO surface is highly basic, *i.e.*, a strong electron donor, while CeO_2 is not. This likely contributes to the higher activity on CeO_2 as well.

As for the ligand effect, we think Ir-PDO/CeO_2 activate H_2 better than Ir-DPTZ/CeO_2, likely because Ir on the former is more electron deficient, as a result of electron tuning by the ligand. Nonetheless, we cannot eliminate geometric effects. Our previous UHV studies exhibit that on Au(100) surface, both ligands favor flat-lying geometries when forming metal-ligand single atoms.[25, 26] Nevertheless, powdered oxide supports have much rougher surfaces and stronger interactions with Ir, making different geometries possible. Ligand geometry can affect the coordination between Ir and reactants sterically. It may also influence the interaction between ligand molecular orbitals and Ir valence orbitals, impacting catalysis indirectly through electronic effects. The ligand effect highlights the extra tunability Ir-ligand SACs have over typical SACs without ligands. As is observed in homogeneous catalysis, the ligand can exert both electronic and geometric effects on the metal center. Inspired by the ligand and support effects, we are

exploring broader ligand space and support engineering strategies to enhance the performance of metal-ligand SACs.

2. Evolution of Ir single atoms under H_2

The behaviors of Ir single atoms under H_2, investigated by H_2-D_2 exchange and *in situ* XAS, are summarized as **Scheme 1**. Fresh Ir single-atoms are not active for H_2 dissociation until activated at elevated temperature under H_2. The activation is accompanied by replacing Ir−O/N and Ir−Cl coordination with Ir−H (**Figs. 7a** and **7d**), which was clearly observed in XAS (**Figs. 7a** and **7d**). This suggests that the detachment of Cl and O/N is required to open coordination vacancies on Ir (initial total CN ≈ 7) for H_2 dissociation. The leaving of Cl is also observed during ethylene hydrogenation (**Tables 2** and **S3**), and in our our previous hydrosilylation experiments over Pt SACs.[30, 31] The loss of O/N coordination could partially arise from the minor PDO desorption (**Table S3**) or C=O detaching from Ir, but should also have contribution from

the breaking of Ir−O bonds at the metal-oxide interface, which has been reported under H_2 on oxide-supported single atoms and NPs.[88-91]

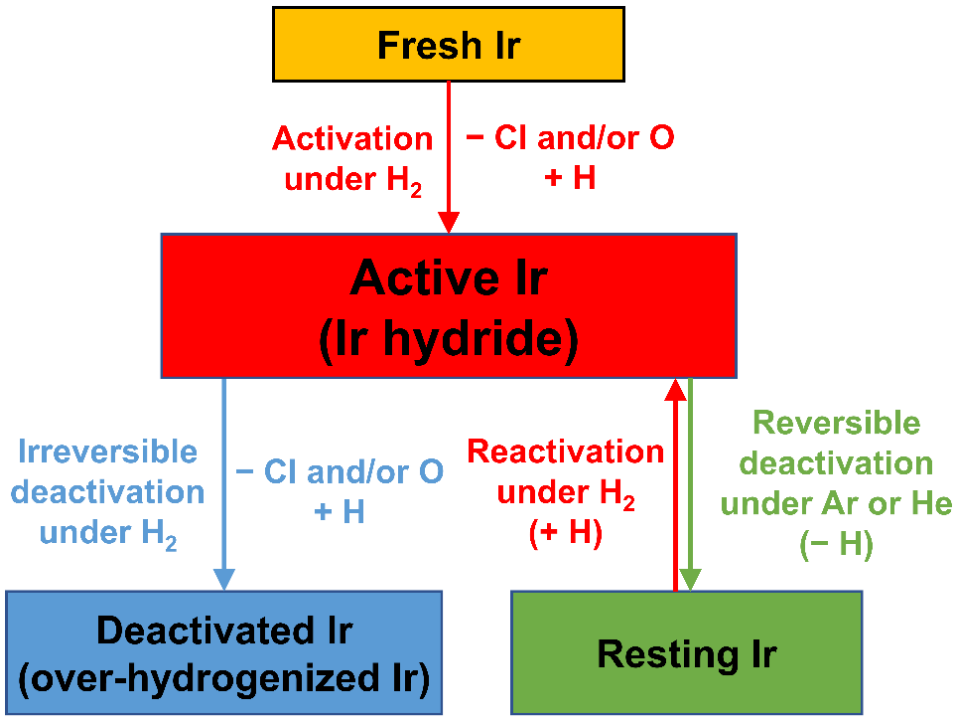

Scheme 1. Summary of various Ir forms observed under H_2 and inert gas treatment.

After the activation of Ir-PDO/MgO, further replacement of Ir−O/N and Ir−Cl by Ir−H coincides with the gradual irreversible deactivation, *i.e.*, the over-hydrogenation of Ir reduces H_2 activation capability. This may be traced back to the electronic effect discussed above: the replacement increases electron density on Ir, as indicated by the white line intensity drop and the absorption edge shifts to higher energy in XANES, and thus decreases H_2 activation capability. The other possibility is that the irreversible deactivation is a direct result of losing Ir−O pairs, the structure proposed to be responsible for H_2 dissociation heterolytically. For comparison, on Ir-PDO/CeO_2, a SAC exhibiting very minor irreversible deactivation, H_2 treatment does not lead to loss of Ir−O/N coordination, implying its correlation with the irreversible deactivation. In

addition, prior studies suggest that H_2 treatment of oxide-supported SACs leads to reduction of support surfaces,[88, 89] which makes heterolytic H_2 dissociation more difficult.[88] This may lead to the irreversible deactivation as well. We emphasize that no clusters/particles are found by EXAFS on any post-reaction or post-H_2 catalysts, and the deactivated Ir are still single-atoms.

Despite relatively quick loss of H_2 activation capability under H_2/D_2 (**Fig. S9**), Ir-PDO/MgO does not deactivate as quickly during ethylene hydrogenation at the same temperature and H_2 partial pressure (**Fig. 5**). This is potentially because on Ir-PDO/MgO, H_2 dissociation is the RDS of ethylene hydrogenation (**Table 3** and **Fig. S7**). Therefore, H does not accumulate under steady-states, avoiding over-hydrogenation and, hence, deactivation. As a result, after 7 h hydrogenation, the Ir reduction and loss of Ir−O/N are significantly less severe (white line intensity = 2.61 and *N*(Ir−O/N) = 5.4 **Table 2**) than after 7 h H_2 treatment (white line intensity = 2.21 and *N*(Ir−O/N) = 1.5, **Fig. 7d**). The comparison shows the durability of Ir-PDO/MgO for H_2 activation can only be maintained when dissociated H are consumed quickly. Therefore, one should be cautious when applying H_2-rich atmospheres to the SACs, to avoid over-hydrogenation and, hence, deactivation.

On the other hand, the reversible deactivation under inert gas and the reactivation under H_2 are associated with the desorption/re-adsorption of H from/onto Ir, without significant changes in *N*(Ir−O/N) and *N*(Ir−Cl). The process is facile, as all spectroscopic changes are completed within 2 h after gas switching at 100 °C (**Figs. 7b-7d**). The reversible deactivation suggests that Ir hydride is the active site necessary for H_2 activation, and the loss of H transforms Ir into an inactive, resting state. When re-introducing H_2, Ir needs to recover the hydride form first, which occurs quickly as suggested by XANES (**Fig. 7d**) to show full H_2 activation capability again, leading to gradual reactivation. We note that only a small fraction of H desorbs/re-adsorbs

from/onto Ir in **Figs. 7b** and **7c**. This could be due to most Ir having been irreversibly deactivated. The reversible deactivation is observed on both SACs and NPs, supported on either CeO_2 or MgO, indicating Ir hydride is the shared active site.

Conclusions

In this work, we applied a metal-ligand complexation strategy to create series of oxide-supported Ir SACs for ethylene hydrogenation. Detailed characterization with XAS, XPS, CO adsorption, TEM, and XRD confirmed that Ir predominantly forms cationic single-atoms binding to the support and the ligand. Ir SACs exhibit higher metal utilization efficiency than supported Ir NPs because of higher metal dispersion and better durability against carbon poisoning. Post-reaction characterization proved that Ir single-atoms are highly stable as no aggregation was detected under reaction conditions. In addition to stabilizing high-density Ir single-atoms, the ligand also allows for desired tunability: hydrogenation activity of Ir SACs is highly sensitive to the ligand and the support, with PDO and CeO_2 outperforming DPTZ and MgO. H_2/D_2 exchange and H_2 reaction order revealed that the ligand and support effects originate from the H_2 dissociation step, which is facilitated by the high reducibility of CeO_2 and the more electron-deficient Ir sites. Investigations of Ir evolution under H_2-inert gas-H_2 treatment suggest Ir hydride formed *in situ* is the active species for H_2 dissociation, but Ir can be deactivated by over-hydrogenation and too much loss of Ir−O/N coordination. This work presents a new class of metal-ligand heterogeneous hydrogenation SACs with excellent metal utilization efficiency, stability, and tunability. The fundamental understanding gained in this work will contribute to further development of efficient and highly selective hydrogenation SACs.

Conflicts of Interest

There are no conflicts of interest to declare.

Acknowledgement

This work was supported by the U. S. Department of Energy (DOE), Office of Basic Energy Sciences, Chemical Sciences program, DE-SC0016367. XPS measurements were carried out at the Indiana University Nanoscale Characterization Facility with assistance from Dr. Yaroslav Losovyj. XAS measurements were performed at beamline 9-BM at the Advanced Photon Source, a U. S. DOE Office of Science User Facility operated for the DOE Office of Science by Argonne National Laboratory under Contract No. DE-AC02-06CH11357. Dr. Tianpin Wu assisted with XAS measurements.

Author ORCiDs

Linxiao Chen	0000-0003-3177-380X
Iyad S. Ali	0000-0001-5671-2304
George E. Sterbinsky	(none)
Xuemei Zhou	0000-0002-3321-3606
Eman Wasim	0000-0002-0373-4371
Steven L. Tait	0000-0001-8251-5232

References

1. Z. Huang, X. Gu, Q. Cao, P. Hu, J. Hao, J. Li and X. Tang, *Angew. Chem.*, 2012, **124**, 4274-4279.
2. E. Fako, Z. Lodziana and N. Lopez, *Catal. Sci. Technol.*, 2017, **7**, 4285-4293.
3. Y. X. Chen, Z. W. Huang, Z. Ma, J. M. Chen and X. F. Tang, *Catal. Sci. Technol.*, 2017, **7**, 4250-4258.
4. B. Qiao, A. Wang, X. Yang, L. F. Allard, Z. Jiang, Y. Cui, J. Liu, J. Li and T. Zhang, *Nature Chem.*, 2011, **3**, 634-641.
5. H. Sohn, J. Camacho-Bunquin, R. R. Langeslay, P. A. Ignacio-de Leon, J. Niklas, O. G. Poluektov, C. Liu, J. G. Connell, D. Yang, J. Kropf, H. Kim, P. C. Stair, M. Ferrandon and M. Delferro, *Chem. Commun.*, 2017, **53**, 7325-7328.
6. J. M. Thomas, *Phys. Chem. Chem. Phys.*, 2014, **16**, 7647-7661.
7. L. Zhong, M.-Y. Lee, Z. Liu, Y.-J. Wanglee, B. Liu and S. L. Scott, *J. Catal.*, 2012, **293**, 1-12.
8. C. Tiozzo, C. Bisio, F. Carniato, A. Gallo, S. L. Scott, R. Psaro and M. Guidotti, *Phys. Chem. Chem. Phys.*, 2013, **15**, 13354-13362.

9. L. A. Williams, N. Guo, A. Motta, M. Delferro, I. L. Fragalà, J. T. Miller and T. J. Marks, *Proc. Natl. Acad. Sci.*, 2013, **110**, 413-418.

10. J. Canivet, S. Aguado, Y. Schuurman and D. Farrusseng, *J. Am. Chem. Soc.*, 2013, **135**, 4195-4198.

11. B. Hu, A. B. Getsoian, N. M. Schweitzer, U. Das, H. Kim, J. Nildas, O. Poluektov, L. A. Curtiss, P. C. Stair, J. T. Miller and A. S. Hock, *J. Catal.*, 2015, **322**, 24-37.

12. G. Vilé, D. Albani, M. Nachtegaal, Z. Chen, D. Dontsova, M. Antonietti, N. López and J. Pérez-Ramírez, *Angew. Chem. Int. Ed.*, 2015, **54**, 11265-11269.

13. W. Xu, B. Yu, Y. Zhang, X. Chen, G. Zhang and Z. Gao, *Appl. Surf. Sci.*, 2015, **325**, 227-234.

14. R. C. Klet, S. Tussupbayev, J. Borycz, J. R. Gallagher, M. M. Stalzer, J. T. Miller, L. Gagliardi, J. T. Hupp, T. J. Marks and C. J. Cramer, *J. Am. Chem. Soc*, 2015, **137**, 15680-15683.

15. J. H. Kwak, J. Hu, D. Mei, C.-W. Yi, D. H. Kim, C. H. F. Peden, L. F. Allard and J. Szanyi, *Science*, 2009, **325**, 1670-1673.

16. M. Boronat, P. Concepción, A. Corma, M. Renz and S. Valencia, *J. Catal.*, 2005, **234**, 111-118.

17. C. M. Osmundsen, M. S. Holm, S. Dahl and E. Taarning, *Proc. Royal Soc. A*, 2012, **468**, 2000-2016.

18. M. D. Marcinkowski, J. Liu, C. J. Murphy, M. L. Liriano, N. A. Wasio, F. R. Lucci, M. Flytzani-Stephanopoulos and E. C. H. Sykes, *ACS Catal.*, 2016, **7**, 413-420.

19. J. Liu, F. R. Lucci, M. Yang, S. Lee, M. D. Marcinkowski, A. J. Therrien, C. T. Williams, E. C. H. Sykes and M. Flytzani-Stephanopoulos, *J. Am. Chem. Soc.*, 2016, **138**, 6396-6399.

20. G. X. Pei, X. Y. Liu, X. Yang, L. Zhang, A. Wang, L. Li, H. Wang, X. Wang and T. Zhang, *ACS Catal.*, 2017, **7**, 1491-1500.

21. G. Kyriakou, M. B. Boucher, A. D. Jewell, E. A. Lewis, T. J. Lawton, A. E. Baber, H. L. Tierney, M. Flytzani-Stephanopoulos and E. C. H. Sykes, *Science*, 2012, **335**, 1209.

22. L. DeRita, S. Dai, K. Lopez-Zepeda, N. Pham, G. W. Graham, X. Pan and P. Christopher, *J. Am. Chem. Soc.*, 2017, **139**, 14150-14165.

23. H. V. Thang, G. Pacchioni, L. DeRita and P. Christopher, *J. Catal.*, 2018, **367**, 104-114.

24. D. Skomski, C. D. Tempas, B. J. Cook, A. V. Polezhaev, K. A. Smith, K. G. Caulton and S. L. Tait, *J. Am. Chem. Soc.*, 2015, **137**, 7898-7902.

25. D. Skomski, C. D. Tempas, G. S. Bukowski, K. A. Smith and S. L. Tait, *J. Chem. Phys.*, 2015, **142**, 101913.

26. D. Skomski, C. D. Tempas, K. A. Smith and S. L. Tait, *J. Am. Chem. Soc.*, 2014, **136**, 9862-9865.

27. C. D. Tempas, T. Morris, D. L. Wisman, D. Le, N. U. Din, C. G. Williams, M. Wang, A. V. Polezhaev, T. S. Rahman, K. G. Caulton and S. L. Tait, *Chem. Sci.*, 2018, **9**, 1674-1685.

28. T. W. Morris, I. J. Huerfano, M. Wang, D. L. Wisman, A. C. Cabelof, N. U. Din, C. D. Tempas, D. Le, A. V. Polezhaev, T. S. Rahman, K. G. Caulton and S. L. Tait, *Chem. Eur. J.*, 2019, **25**, 5565-5573.

29. C. G. Williams, M. Wang, D. Skomski, C. D. Tempas, L. L. Kesmodel and S. L. Tait, *J. Phys. Chem. C*, 2017, **121**, 13183-13190.

30. L. X. Chen, G. E. Sterbinsky and S. L. Tait, *J. Catal.*, 2018, **365**, 303-312.

31. L. Chen, I. S. Ali, G. E. Sterbinsky, J. T. L. Gamler, S. E. Skrabalak and S. L. Tait, *ChemCatChem*, 2019, **11**, 2843-2854.

32. M. J. Climent, A. Corma and S. Iborra, *Green Chemistry*, 2014, **16**, 516-547.

33. E. L. Kunkes, D. A. Simonetti, R. M. West, J. C. Serrano-Ruiz, C. A. Gartner and J. A. Dumesic, *Science*, 2008, **322**, 417-421.

34. W. Wang, S. P. Wang, X. B. Ma and J. L. Gong, *Chem. Soc. Rev.*, 2011, **40**, 3703-3727.

35. J. A. Rodriguez, D. C. Grinter, Z. Y. Liu, R. M. Palomino and S. D. Senanayake, *Chem. Soc. Rev.*, 2017, **46**, 1824-1841.

36. R. Mariscal, P. Maireles-Torres, M. Ojeda, I. Sadaba and M. L. Granados, *Energy & Environmental Science*, 2016, **9**, 1144-1189.

37. R. A. Sheldon, *Green Chemistry*, 2014, **16**, 950-963.

38. B. Chen, U. Dingerdissen, J. G. E. Krauter, H. Rotgerink, K. Mobus, D. J. Ostgard, P. Panster, T. H. Riermeier, S. Seebald, T. Tacke and H. Trauthwein, *Appl. Catal. A*, 2005, **280**, 17-46.

39. H. U. Blaser, C. Malan, B. Pugin, F. Spindler, H. Steiner and M. Studer, *Adv. Synth. Catal.*, 2003, **345**, 103-151.

40. J. A. Widegren and R. G. Finke, *J. Molec. Catal. A*, 2003, **198**, 317-341.

41. R. Noyori and T. Ohkuma, *Angew. Chem. Int. Ed.*, 2001, **40**, 40-73.

42. M. L. M. Bonati, T. M. Douglas, S. Gaemers and N. Guo, *Organometallics*, 2012, **31**, 5243-5251.

43. F. Huang, Y. C. Deng, Y. L. Chen, X. B. Cai, M. Peng, Z. M. Jia, P. J. Ren, D. Q. Xiao, X. D. Wen, N. Wang, H. Y. Liu and D. Ma, *J. Am. Chem. Soc.*, 2018, **140**, 13142-13146.

44. J. Lu, P. Serna, C. Aydin, N. D. Browning and B. C. Gates, *J. Am. Chem. Soc.*, 2011, **133**, 16186-16195.

45. M. Babucci, C. Y. Fang, A. S. Hoffman, S. R. Bare, B. C. Gates and A. Uzun, *ACS Catal.*, 2017, **7**, 6969-6972.

46. A. S. Hoffman, L. M. Debefve, S. J. Zhang, J. E. Perez-Aguilar, E. T. Conley, K. R. Justl, I. Arslan, D. A. Dixon and B. C. Gatesr, *ACS Catal.*, 2018, **8**, 3489-3498.

47. M. Babucci, C.-Y. Fang, J. E. Perez-Aguilar, A. S. Hoffman, A. Boubnov, E. Guan, S. R. Bare, B. C. Gates and A. Uzun, *Chem. Sci.*, 2019, **10**, 2623-2632.

48. Z. H. Syed, D. M. Kaphan, F. A. Perras, M. Pruski, M. S. Ferrandon, E. C. Wegener, G. Celik, J. Wen, C. Liu, F. Dogan, K. I. Goldberg and M. Delferro, *J. Am. Chem. Soc.*, 2019, **141**, 6325-6337.

49. N. M. Schweitzer, B. Hu, U. Das, H. Kim, J. Greeley, L. A. Curtiss, P. C. Stair, J. T. Miller and A. S. Hock, *ACS Catal.*, 2014, **4**, 1091-1098.

50. P. Ji, K. Manna, Z. Lin, A. Urban, F. X. Greene, G. Lan and W. Lin, *J. Am. Chem. Soc.*, 2016, **138**, 12234-12242.

51. P. F. Ji, Y. Song, T. Drake, S. S. Veroneau, Z. K. Lin, X. D. Pan and W. B. Lin, *J. Am. Chem. Soc.*, 2018, **140**, 433-440.

52. Y. Xu, M. A. Celik, A. L. Thompson, H. Cai, M. Yurtsever, B. Odell, J. C. Green, D. M. P. Mingos and J. M. Brown, *Angew. Chem. Int. Ed.*, 2009, **48**, 582-585.

53. P. Brandt, C. Hedberg and P. G. Andersson, *Chem. Eur. J.*, 2003, **9**, 339-347.

54. K. Kallstrom, I. Munslow and P. G. Andersson, *Chem. Eur. J.*, 2006, **12**, 3194-3200.

55. D. S. Wang, J. Zhou, D. W. Wang, Y. L. Guo and Y. G. Zhou, *Tetrahedron Letters*, 2010, **51**, 525-528.

56. T. M. Gilbert, F. J. Hollander and R. G. Bergman, *J. Am. Chem. Soc.*, 1985, **107**, 3508-3516.

57. S. P. Smidt, A. Pfaltz, E. Martinez-Viviente, P. S. Pregosin and A. Albinati, *Organometallics*, 2003, **22**, 1000-1009.

58. Z. Jakub, J. Hulva, M. Meier, R. Bliem, F. Kraushofer, M. Setvin, M. Schmid, U. Diebold, C. Franchini and G. S. Parkinson, *Angew. Chem. Int. Ed.*, 2019, **58**, 13961-13968.

59. B. Ravel and M. Newville, *J. Synch. Rad.*, 2005, **12**, 537-541.

60. L. Chen, J. P. McCann and S. L. Tait, *Appl. Catal. A*, 2018, **549**, 19-30.

61. L. Chen, V. Agrawal and S. L. Tait, *Catal. Sci. Technol.*, 2019, **9**, 1802-1815.

62. A. Bruix, J. A. Rodriguez, P. J. Ramírez, S. D. Senanayake, J. Evans, J. B. Park, D. Stacchiola, P. Liu, J. Hrbek and F. Illas, *J. Am. Chem. Soc.*, 2012, **134**, 8968-8974.

63. J. Lu, P. Serna and B. C. Gates, *ACS Catal.*, 2011, **1**, 1549-1561.

64. L. Chen, G. E. Sterbinsky and S. L. Tait, *J. Catal.*, 2018, **365**, 303-312.

65. F. Solymosi, E. Novak and A. Molnar, *J. Phys. Chem.*, 1990, **94**, 7250-7255.

66. A. Bourane, M. Nawdali and D. Bianchi, *J. Phys. Chem. B*, 2002, **106**, 2665-2671.

67. A. Erdo˝helyi, K. Fodor and G. Suru, *Appl. Catal. A*, 1996, **139**, 131-147.

68. G. Kisters, J. G. Chen, S. Lehwald and H. Ibach, *Surf. Sci.*, 1991, **245**, 65-71.

69. P. Gélin, A. Auroux, Y. B. Taarit and P. C. Gravelle, *Applied Catalysis*, 1989, **46**, 227-240.

70. B. Sheludko, M. T. Cunningham, A. S. Goldman and F. E. Celik, *ACS Catal.*, 2018, **8**, 7828-7841.

71. P. Gelin, G. Coudurier, Y. B. Taarit and C. Naccache, *J. Catal.*, 1981, **70**, 32-40.

72. A. Wieckowski, S. D. Rosasco, G. N. Salaita, A. Hubbard, B. E. Bent, F. Zaera, D. Godbey and G. A. Somorjai, *J. Am. Chem. Soc.*, 1985, **107**, 5910-5920.

73. A. Tillekaratne, J. P. Simonovis and F. Zaera, *Surf. Sci.*, 2016, **652**, 134-141.

74. P. S. Cremer, X. C. Su, Y. R. Shen and G. A. Somorjai, *J. Am. Chem. Soc.*, 1996, **118**, 2942-2949.

75. T. Ohtani, J. Kubota, J. N. Kondo, C. Hirose and K. Domen, *J. Phys. Chem. B*, 1999, **103**, 4562-4565.

76. A. Dervisi, C. Carcedo and L. Ooi, *Adv. Synth. Catal.*, 2006, **348**, 175-183.

77. F. R. Lucci, J. Liu, M. D. Marcinkowski, M. Yang, L. F. Allard, M. Flytzani-Stephanopoulos and E. C. H. Sykes, *Nature Comm.*, 2015, **6**, 8550.

78. K. A. Woerpel and R. G. Bergman, *J. Am. Chem. Soc.*, 1993, **115**, 7888-7889.

79. B. A. Morrow and P. Ramamurthy, *J. Phys. Chem.*, 1973, **77**, 3052-3058.

80. Q. Zhang, Z. Song, P. Ning, X. Liu, H. Li and J. Gu, *Catal. Comm.*, 2015, **59**, 170-174.

81. X. Du, L. Dong, C. Li, Y. Liang and Y. Chen, *Langmuir*, 1999, **15**, 1693-1697.

82. L. Yue and X.-M. Zhang, *J. Alloys Compounds*, 2009, **475**, 702-705.

83. F. C. Meunier, D. Tibiletti, A. Goguet, D. Reid and R. Burch, *Appl. Catal. A*, 2005, **289**, 104-112.

84. M. W. Tew, J. T. Miller and J. A. van Bokhoven, *J. Phys. Chem. C*, 2009, **113**, 15140-15147.

85. S. Mukerjee and J. McBreen, *J. Electrochem. Soc.*, 1999, **146**, 600-606.

86. A. L. Ankudinov, J. J. Rehr, J. Low and S. R. Bare, *Phys. Rev. Lett.*, 2001, **86**, 1642-1645.

87. Y. Lei, J. Jelic, L. C. Nitsche, R. Meyer and J. Miller, *Top. Catal.*, 2011, **54**, 334-348.

88. N. Doudin, S. F. Yuk, M. D. Marcinkowski, M.-T. Nguyen, J.-C. Liu, Y. Wang, Z. Novotny, B. D. Kay, J. Li, V.-A. Glezakou, G. Parkinson, R. Rousseau and Z. Dohnálek, *ACS Catal.*, 2019, **9**, 7876-7887.

89. R. Bliem, J. van der Hoeven, A. Zavodny, O. Gamba, J. Pavelec, P. E. de Jongh, M. Schmid, U. Diebold and G. S. Parkinson, *Angew. Chem. Int. Ed.*, 2015, **54**, 13999-14002.

90. D. C. Koningsberger and B. C. Gates, *Catal Lett*, 1992, **14**, 271-277.

91. N. C. Nelson, M.-T. Nguyen, V.-A. Glezakou, R. Rousseau and J. Szanyi, *Nature Catal.*, 2019, **2**, 916-924.